The 3D Q_P Model of the China Seismic Experiment Site (CSES-Q1.0) and Its Tectonic Implications

Mengqiao Duan[1] Lianqing Zhou[1*] Ying Fu[2] Yanru An[3] Jingqiong Yang[4] Xiaodong Zhang[1]

[1]Institute of Earthquake Forecasting, China Earthquake Administration, Beijing 100036, China
5   [2]Sichuan Earthquake Administration, Chengdu, 61004, China
[3]China Earthquake Networks Center, China Earthquake Administration, Beijing 100045, China
[4]Yunnan Earthquake Administration, Kunming, 650224, China

Correspondence to: Lianqing Zhou (zhoulq@ief.ac.cn)

Abstract. The Chuan-Dian region is located in the southeastern part of the geologically complex and seismically active
10   Tibetan Plateau. Since 2008, the Chuan-Dian region has experienced several major earthquakes, including the Wenchuan M_S 8.0, Lushan M_S 7.0, and Jiuzhaigou M_S7.0, making it one of the areas with the most severe earthquake disasters. The China Seismic Experimental Site (CSES) under construction in this area will deepen the understanding of the preparation and generation of earthquakes and the disaster mechanisms, which can further enhance the defense capability against earthquake risks. To build a world-class seismic experimental field, it is necessary to establish high-precision
15   medium structure models. Currently, several institutions have established high-resolution three-dimensional (3D) velocity models in the CSES, but there is still a lack of high-resolution 3D attenuation ($\propto 1/Q$) structure models. Using the local seismic tomography method, we obtain the highest resolution 3D Q_P model in the CSES to date. Combining the existing velocity models in the CSES with other geophysical and geochemical observations by predecessors, this study shows that the Q_P value anomalies along large fault zones and some basin areas are low, reflecting the high degree of medium
20   fragmentation in these areas, with thick sedimentary layers or rich in fluids. The high attenuation anomaly of the upper crust dipping westward in the Tengchong volcanic characterizes the possible upward flow of deep-seated magma from west to east. This study also reveals that most of earthquakes above magnitude 6 occurred in low attenuation zones or the boundary areas of high-low attenuation anomalies. The source areas of the 2008 Wenchuan Ms 8.0 earthquake and the 2013 Lushan Ms 7.0 earthquake were separated by a low attenuation area, and there is still a risk of major earthquakes in the future. The
25   3D attenuation model constructed in this study will provide a high-resolution reference model for seismological and earthquake disaster research in the CSES.

1 Introduction

The China Seismic Experimental Site (CSES) started construction in 2018 (regional range: 97.5°-105.5°E, 21°-32°N), with a total area of approximately 780,000 square kilometers. The regional scope includes the Chuan-Dian block (CDB) located on

30 the southeastern Tibet Plateau and its surrounding areas, with a complex tectonic environment and various fault systems such as compression, shear, and tension. Multiple large thrust and strike-slip active fault zones have developed in the region, such as the Xianshuihe, Zemuhe, Xiaojiang, Red River, Longmenshan, Huayingshan, and Lijiang-Xiaojinhe fault zones. They divide the Chuan-Dian area into multiple active blocks, such as the Chuan-dian block, the Western Yunnan block, the Southern Yunnan block. (Zhang et al., 2003) (Fig. 1a). The collision and continuous convergence of the Indian and Eurasian

35 plates led to strong crustal deformation and rapid surface uplift. This region is also one of the regions with the most frequent seismicity in Chinese Mainland, including both interplate and intraplate earthquakes. In the past 50 years, there have been an average of 14 earthquakes with a magnitude of 6.0 or above and 3 earthquakes with a magnitude of 7.0 or above every 10 years (Fig. 1b). Among them, the Wenchuan 8.0 earthquake on May 12, 2008, the Lushan 7.0 earthquake on April 20, 2013, the Ludian 6.5 earthquake on August 3, 2014, the Yangbi 6.4 earthquake on May 21, 2021, and the Luding 6.8 earthquake on

40 September 5, 2022 all caused serious casualties and property losses. The seismogenic environment and mechanism in this region have always been a hot topic of discussion among scholars. Previously, various geophysical observations, such as low wave velocity (Yao et al., 2008; Yang et al., 2012, 2020; Bao et al., 2015; Zhang et al., 2020; Liu et al., 2021), high conductivity (Bai et al., 2010; Li et al., 2019), high heat flow (Hu et al., 2000; Jiang et al., 2019), strong attenuation (Zhao et al., 2013) and strong radial anisotropy (Bao et al., 2020) reveal the morphology and genesis of channel flows in the middle

45 and lower crust. Among them, research on 3D velocity tomography is dominant, including 3D velocity structures based on body waves (Wu et al., 2013; Deng et al., 2021; Wang et al., 2015;Huang et al., 2018).Three dimensional V_S structure of the crust to upper mantle based on surface waves and background noise (Wang and Gao, 2014; Yao et al., 2008; Shen et al., 2016; Fu et al., 2017; Qiao et al., 2018; Zheng et al., 2019; Yang et al., 2020).

To investigate the high-resolution subsurface medium structure of the CSES and understand the mechanisms of strong

50 earthquakes in the region, seismologists have constructed various velocity models for CSES using various data, including body waves, surface waves, and ambient noise surface waves. For instance, Xin et al. (2019) and Han et al. (2022) successively used the inversion method of body waves and joint inversion method of body- and surface-wave to establish high-resolution lithospheric velocity structures for the Chinese mainland (USTClitho1.0, USTClitho2.0), with horizontal resolutions in the CSES ranging from 0.5° to 1°. Liu et al. (2021) and Liu et al. (2023) utilized joint body- and surface-wave

55 travel-time inversion method to establish two community velocity models for CSES (SWChinaCVM-1.0, SWChinaCVM-2.0), with the maximum horizontal resolution of 0.2-0.3°, providing high-resolution community velocity models for geophysics research in the CSES area. The most recent study, based on the joint inversion of receiver functions and surface waves, constructed a 3D V_P and V_S model for CSES (CSES-VM1.0) with a maximum horizontal resolution of 0.25° (Wu et al., 2024). However, the velocity structure mainly reflects the elastic structure of the medium and lacks constraints on

60 important inelastic properties during earthquake nucleation.
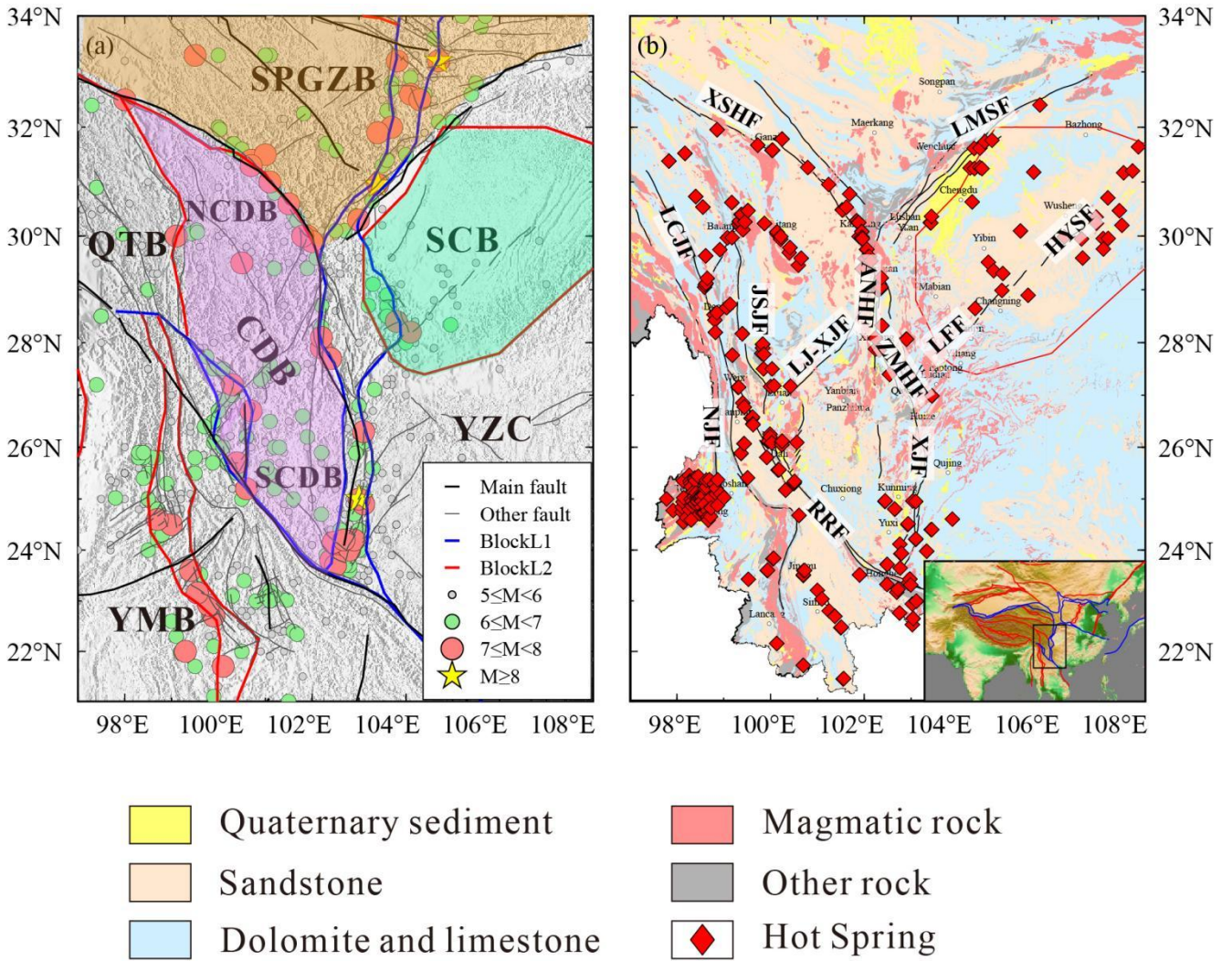
Figure 1: The distribution map of tectonic structures, historical earthquakes, and lithology in the study area.

(a) Map of the tectonic structures and spatial distribution of earthquakes occurred from 780 BC to July 2023 in the CSES. SPGZB, Songpan-Ganze Block; QTB, Qiangtang Block; CDB, Chuan-Dian Block; NCDB, Southern Chuan-Dian Block; SCDB, Southern Chuan-Dian Block; YMB, Yunnan-Myanmar Block; SCB, Sichuan Basin; YZC, Yangtze Craton.

(b) Map of the spatial distribution of lithology and hot springs in the CSES. XSHF, Xianshuihe fault; LMSF, Longmenshan fault; ANHF, Anninghe fault; ZMHF, Zemuhe fault; XJF, Xiaojiang fault; HYSF, Huayingshan fault; LFF, Lianfeng fault; JSJF, Jinshajiang fault, LJ-XJHF, Lijiang-Xiaojinhe fault; LCJF, Lancangjiang fault; NJF, Nujiang fault.

Seismic wave attenuation is an important parameter reflecting the inelastic properties of the medium. Seismic wave attenuation is typically extracted from the amplitudes of seismic waves (Pei et al., 2010) and is inversely proportional to the quality factor Q. The state of fractures, fluid migration, and thermal material upwelling in the medium can all cause variations in Q (Yang et al., 2007; Zhu et al., 2013; Wang et al., 2017; Chen et al., 2021). Compared to seismic wave velocities, seismic wave attenuation is more sensitive to changes in fluids and temperature (Lin, 2014; Guo and Thurber,

2022). It can provide better constraints on the physical state of the medium and more important information for the thermal structure and dynamics of the lithosphere (Deng et al., 2021), and help us infer the permeability range of fluids and the the heterogeneity of thermal structures. Studies have also found that most moderate and strong earthquakes (magnitude 6 and above) in the Chuan-Dian region occur at the boundaries of high attenuation or high-low attenuation anomalies (Zhou et al., 2008; Zhou et al., 2020). Therefore, attenuation structures can also provide scientific reference for the determination of the locations of large earthquakes.

At present, most attenuation models in the Chuan-Dian region are two-dimensional models of Lg waves or surface waves, which cannot accurately reveal the characteristics of attenuation in depth (Zhou et al., 2008; Zhao et al., 2013; Wei et al., 2019; Zhou et al., 2020). There are few published studies on 3D attenuation structures in the CSES and surrounding areas. Dai et al. (2020) only obtained a 3D body wave attenuation model for the southeastern part of the Chuan-Dian block, with low resolution. Tang et al. (2023) inverted a 3D shear wave attenuation model below a depth of 30 km, lacking the 3D attenuation structure of the upper and middle crust. Liu et al. (2024) used teleseismic direct-P waves to obtain crustal and upper mantle attenuation structure beneath the southeastern Tibetan Plateau, but there are only two layers at a depth of 100 km and 200 km. Therefore, CSES still lacks a high-precision crustal 3D attenuation model.

This paper collects a large number of seismic waveforms in CSES over the past decade and uses local earthquake tomography to construct a high-resolution 3D P-wave attenuation model for CSES. Combined with the existing 3D velocity models in CSES, we can better understand the medium properties and seismogenic environment in CSES. It will provide a scientific basis for the crustal medium properties of the Tibetan Plateau, the mechanism of crustal material migration, and the assessment of the risk of large earthquakes.

2 Data and Method

2.1 Data

This study collates seismic catalogs, phase reports, and seismic waveforms from earthquakes with magnitudes greater than 1.5, recorded by a total of 582 stations from the Sichuan and Yunnan seismic networks within the study area (21°N -34°N, 97°E -108°E) since 2013. We select events that include at least six both P and S phases and picked phases with travel time residuals within ±2 seconds based on the travel time curves, and a total of 79,619 events from Sichuan and 39,668 events from Yunnan are selected. Due to the fact that earthquakes in Sichuan are more frequent and mainly concentrated around the Longmenshan fault zone, the difference in ray density may result in significant variations in ray weights across different grids. To ensure the resolution of the Q model and to uniformly cover the entire study area with rays, we clustered earthquakes in the Sichuan region, retaining only one earthquake within a 0.5 km range centered on each earthquake. Finally, we organized waveforms for 17,290 earthquakes in Sichuan and 18,488 earthquakes in Yunnan, with a total of 288,695 P-wave rays. The distribution of earthquakes before and after clustering in the region is shown in Fig. 2.
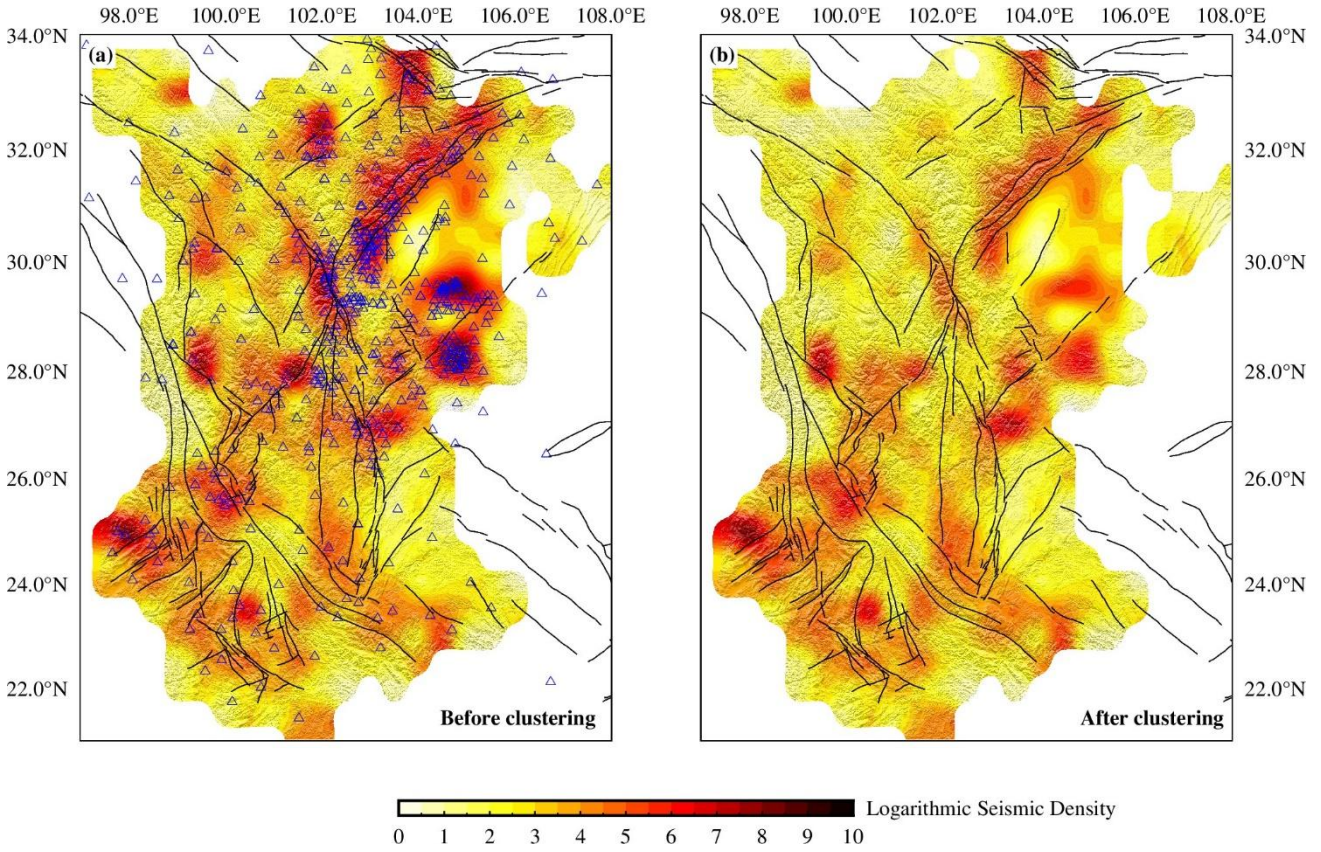
Figure 2: Spatial distribution of logarithmic seismic density in the study area before (a) and after (b) clustering. The blue-framed triangles represent stations.

2.2 Method

110 The seismic wave attenuation conforms to the ω^2 model (Brune, 1970), whose velocity amplitude spectrum can be expressed as follows:

$$A_{ij}(f) = 2\pi f \cdot \frac{\Omega_{0ij} \cdot f_{ci}^2}{f_{ci}^2 + f^2} e^{-\pi f t_{ij}^*}$$

(1)

(1) in which Ω_{0ij} is the spectral level at low frequency of the i-th earthquake recorded by the j-th station, t_{ij}^* is the whole

115 path attenuation term t/Q, f_{ci} is the corner frequency of the event i. Many laboratory and empirical studies found $Q = Q_0 f^\alpha$ (Karato and Spetzler, 1990; McNamara, 2000; Stachnik et al., 2004), where frequency-dependent factor α is usually in the range from 0 to 1. Some studies have found that the frequency-independent Q images are quite similar to the frequency-dependent Q images (Liu and Zhao, 2015; Wang et al., 2017). In this paper, we cannot solve for α, referring to the method of Eberhart-Phillips and Chadwick (2002), and we assume Q value is frequency-independent ($\alpha = 0$). The following steps are

120 used to extract the t* within the frequency range of 2-20 Hz: (1) A flexible window method is used to cut the signal and

noise windows of P waves (Zhou et al., 2011). For the P wave, the vertical component recording is selected. We have referenced several studies which show that t* estimation often used the fixed time window such as 2.56 s after the P-wave onset to calculate the observed velocity spectra of P waves and fit t* (Lees & Lindley1994; Eberhart-Phillips and Chadwick 2002; Hauksson and Shearer, 2006). Some earthquakes have epicentral distances of less than 20 km, and the S-P traveltime

125   differences are less than 2.56 s. When the S-P arrival time difference is less than or equal to 2.56 s, the S-P arrival time difference is used as the signal window of the P wave, and the records whose S-P arrival time difference between is less than 0.5 s are removed. When the S-P arrival time difference is greater than 2.56 s, 2.56 s is selected as the signal window of the P wave, and the noise window is set to 2.56 s before the P wave arrival time. (2) After removing the instrument response, the velocity spectra of the signal and noise are calculated, and the records with a signal-to-noise ratio greater than 2 are selected.

130   (3) For all records of an event, use a grid search method within a certain frequency range to solve for the corner frequency of each event f_{ci}. Specifically, from 2 Hz to 20 Hz at intervals of 0.1 Hz, continuously increase the value of f_{ci} and calculate the theoretical velocity spectrum $D_{ij}(f)$. Assume an initial value of t_{ij}^* is 0.02, fix f_{ci} and an estimated value t_{ij}^*, and use the following formula to calculate the zero-frequency spectral value Ω_{0ij}:

$$\Omega_{0ij} = \frac{\sum_{f<f_{ci}} D_{ij}(f)*A_{ij}(f)}{\sum_{f<f_{ci}} A_{ij}(f)*A_{ij}(f)} \tag{2}$$

135   In which $A_{ij}(f)$ is the theoretical velocity spectrum,$D_{ij}(f)$ is the observed velocity spectrum. (4) By fixing Ω_{0ij} and f_{ci}, a better t_{ij}^* can be obtained:

$$t_{ij}^* = \frac{\sum \log(A_{ij}(f))*f - \sum \log(D_{ij}(f))*f}{\pi \sum f*f} \tag{3}$$

An iterative algorithm is used to fit Ω_{0ij} and t_{ij}^*. Repeating steps (3) and (4) for n iterations, each iteration obtaining a new t_{ij}^* and recalculating Ω_{0ij}. The corner frequency f_{ci} for the event i is determined by the frequency that minimizes the

140   fitting error between the theoretical and the observed velocity spectrum. The expression for the fitting error is:

$$fit = \frac{1}{N}\sum_{n=1}^{N} \log[A_{ij}(f) - D_{ij}(f)]^2 \tag{4}$$

The t* values are also weighted at a total of 5 levels (0, 1, 2, 3, 4) according to the fitting quality, in which 0, 1, 2, 3 represent the fit values with the fitting error less than 0.1, 0.2, 0.3 and 0.4, respectively. Ultimately, we retain data with t* levels less than 4, and ensure that each event has at least 3 t* data. we obtained a total of 176,105 t* data for P waves. Below is an

145   example of t* fitting. (Fig. 3).
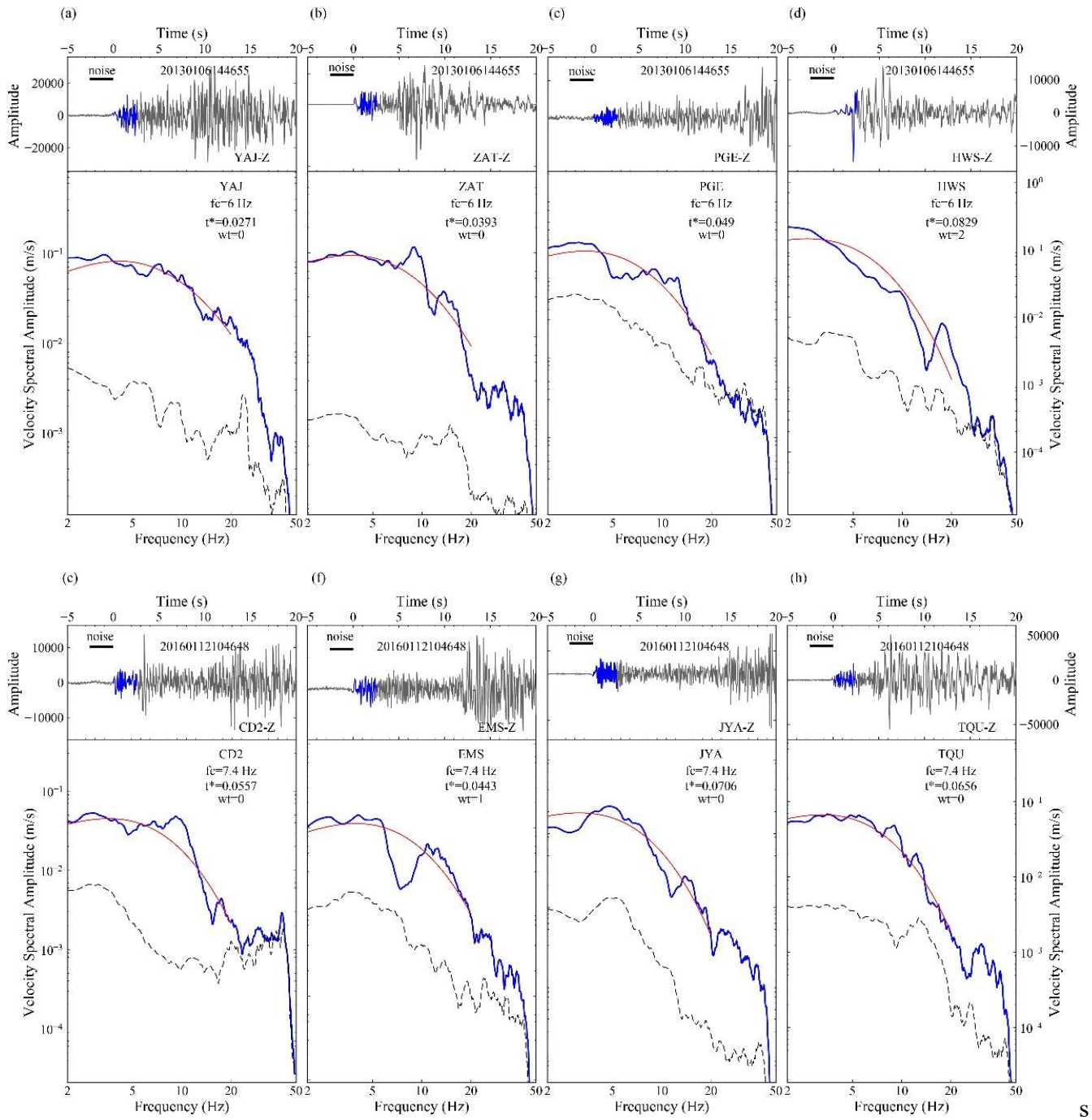
Figure 3: t* fitting example.

The fitting maps of P-wave t* at different stations for the Yunnan Yiliang M_L 3.4 earthquake on January 6, 2013 (a-d), and the Lushan M_L 3.4 earthquake on January 12, 2016 (e-h).

150

t* fitting results of the P-wave. In the upper subfigures, the black wavy lines represent waveforms at different stations from 5 s before to 20 s after the original time, the blue wavy lines represent the P-wave signal windows, and the short black horizontal lines represent the the P-wave noise windows. In the lower subfigures, the blue curves represent the signal velocity spectra, the black dotted lines represent the noise velocity spectra, and the red curves represent the fitted curves. Letters from top to bottom
155 **represent station names, corner frequency, t* values, and weights.**

Then we select the V_P model of SWChinaCVM-1.0 constructed by Liu et al. (2021) to further invert the 3D Q_P model of the region by using the iterative least squares algorithm and SIMUL2000 program (Eberhart-Phillips, 1986; Thurber, 1993; Evans et al., 1994; Eberhart-Phillips and Michael, 1998).

$$t^* = \int_{ray\ path} \frac{1}{Q(s)*V(s)} ds \tag{2}$$

160 We set maximum number of iterations to 10 to perform inversions with Q values between 50 and 650. According to the minimum value of data variance, the initial values of Q_P was set to 350 with 9 iterations. Then, according to the trade-off curve between the model variance and the data variance from the inversion with a single iteration, the optimal damping values of Q_P tomography was set to 0.1. During the inversion, the weight of P-wave with a epicentral distance within 50 km is 1, the weight of P-wave with a epicentral distance between 50 and 200 km linearly changes from 1 to 0, and the weight of 165 P-wave above 200 km is 0. After 6 iterations, the data variance decreased by 46%. The resolution of the final Q_P model also needs to be comprehensively evaluated in combination with checkerboard tests and the spread function (SF) values based on the full resolution matrix. The latter is a better way to identify the resolution than solely examining the diagonal element because diagonal resolution is strongly dependent on the grid spacing and the damping (Reyners et al.,1999).

3 Results

170 ### 3.1 Checkerboard tests

We divide the study area into 0.25º × 0.25ºgrids with depth layers of 0, 5, 10, 15, 20, 25, and 30 km. The initial velocity values of the corresponding grid points are obtained by interpolation based on the SWChinaCVM-1.0. We will first evaluate the resolution of the Q_P model based on the checkerboard test method. We add 5% random noise to the data and add ±20% perturbation to the initial Q value. The checkerboard test results show that the checkerboard with a grid of 50 km×50 km 175 only recovers well at a depth of 10 km, with the Q_P model in Changning area of Sichuan Basin and western Yunnan reaching a lateral resolution of 50 km at a depth of 10 km. The checkerboard test results of a 100 km×100 km grid (Fig. 4) show that the Q_P model recovers well in the Sichuan Basin at a depth of 5 km, and overall recovers well in the study area at depths of 10 km and 15 km. The resolution is poor below 0 km and 20 km. The vertical profiles of Q_P models along different latitudes (Fig. 5) show that the Q_P model in Sichuan can recover well within a depth of 20 km, while the Q_P model in Yunnan can 180 recover well within a depth of 18 km. Therefore, the horizontal resolution of the 3D Q_P model established in this paper for CSES is 100 km, and the vertical resolution is 5 km.
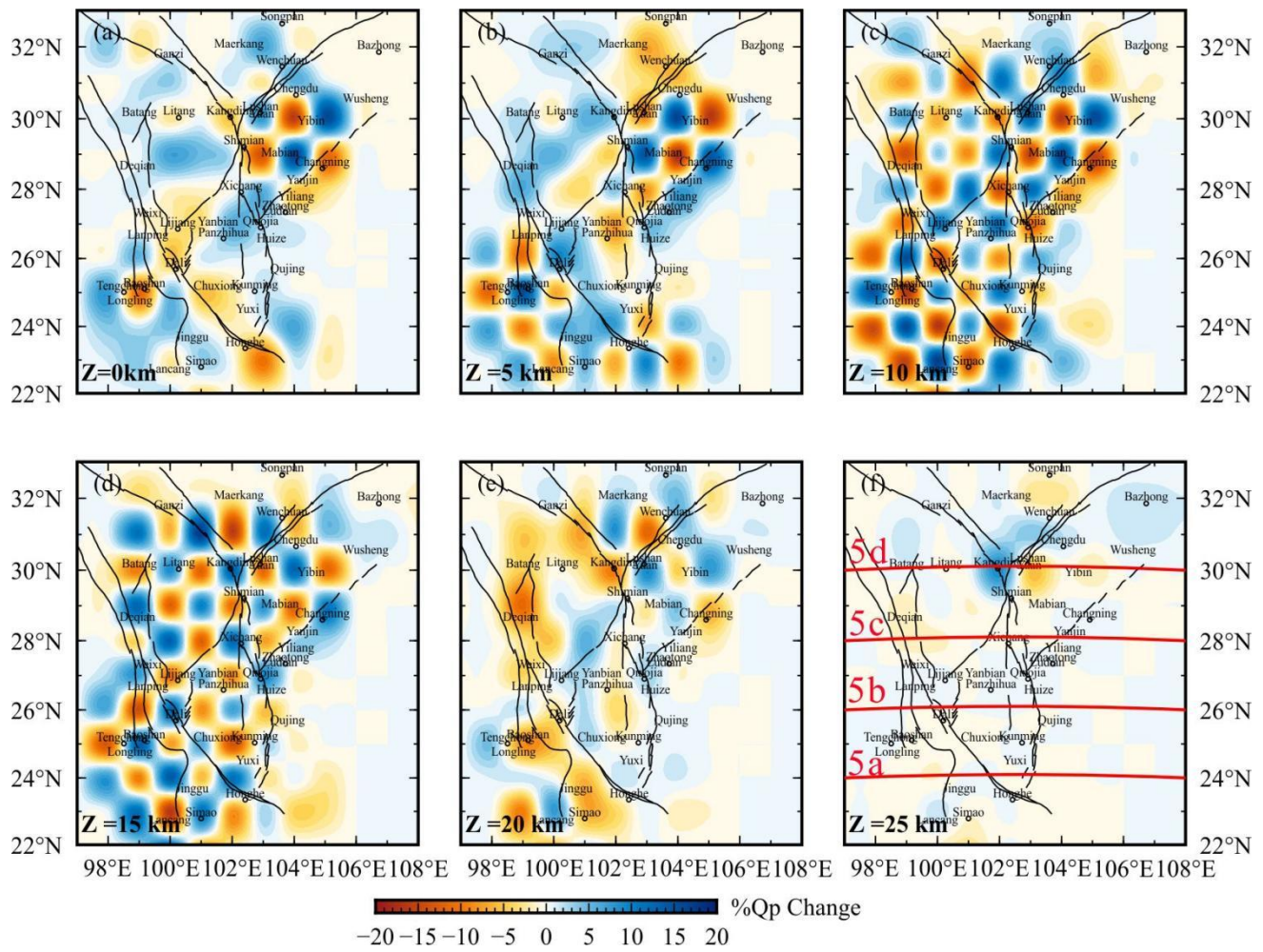
Figure 4: Checkerboard test results of the layered Q_P model.

185 **The red solid line in (f) corresponds to each profile in Figure 5, and the letters above correspond to the numbers in Figure 5.**
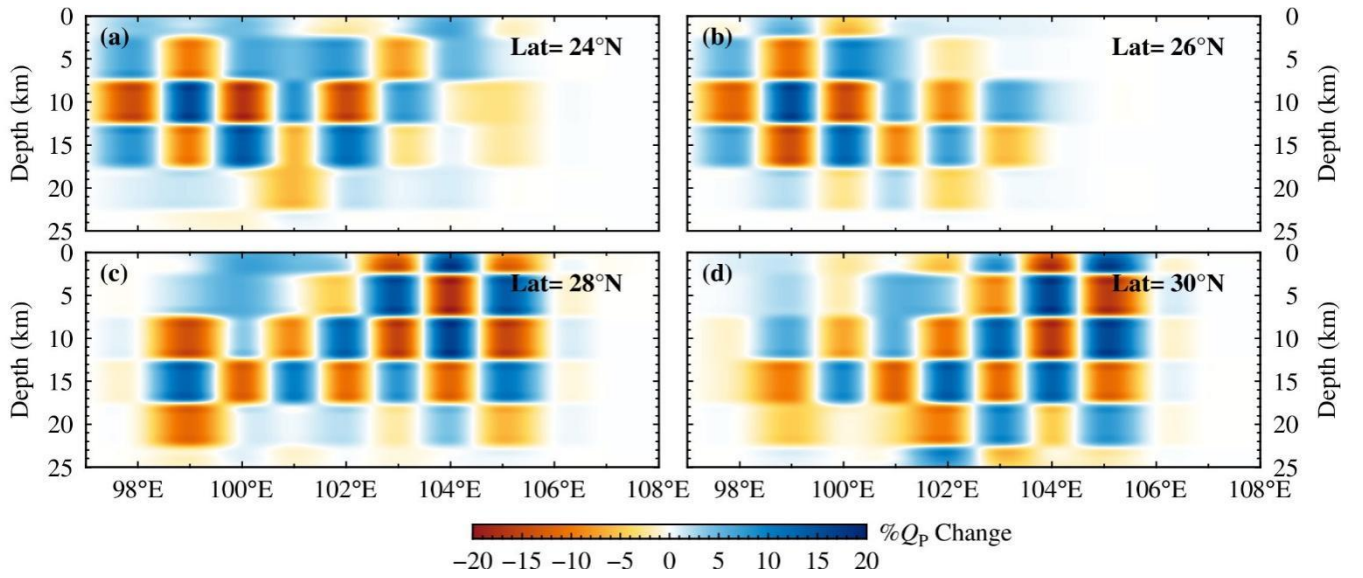
Figure 5: Depth profile of Q_P model along different latitudes in the checkerboard test.

3.2 Resolution tests

190   Referring to the practices of previous researchers (Eberhart Phillips et al., 2008; Zhou et al., 2018; Duan et al., 2024), we further calculate the SF values for each grid point from all the elements of the corresponding row of the resolution matrix to better evaluate the model resolution. Toomey and Foulger (1989) explain that the spread functions does not depend on grid spacing and damping. The quality of resolution is inversely proportional to the SF value, and it is generally used SF ≤ 4 as regions of acceptale Q model quality (Eberhart Phillips and Michael, 1998). If SF > 4, it indicates that the Q model

195   resolution is low and can only present rough features. We fix the Q_P value of grid points with a number of rays less than 5 and obtain the layered SF image of the Q_P model. The results show (Fig. 6) that, except for the Yangtze block, the SF values in most areas at depths of 5 km, 10 km and 15 km are less than 3, indicating that the Chuan-Dian region has better resolution at depths of 10 km and 15 km. At depths of 0 km, the southwestern Sichuan region has good resolution. At a depth of 20 km, the Sichuan Basin and western Yunnan region have good resolution. The SF profile of the Q_P model along the latitude

200   direction (Fig. 7) shows that the resolution of the Q_P model is relatively high in most areas of Sichuan and western Yunnan at depths of about 23 km.

    Integrating the results of the checkerboard test and the SF values for multiple resolution evaluations, we believe that the Q model with SF < 4 in the study area is reliable. The SF ≥ 4 indicates little or no information, and the associated Q model close to the initial model. The following will focus on the Q_P model with SF < 4 within a depth range of 5-20 km.

205
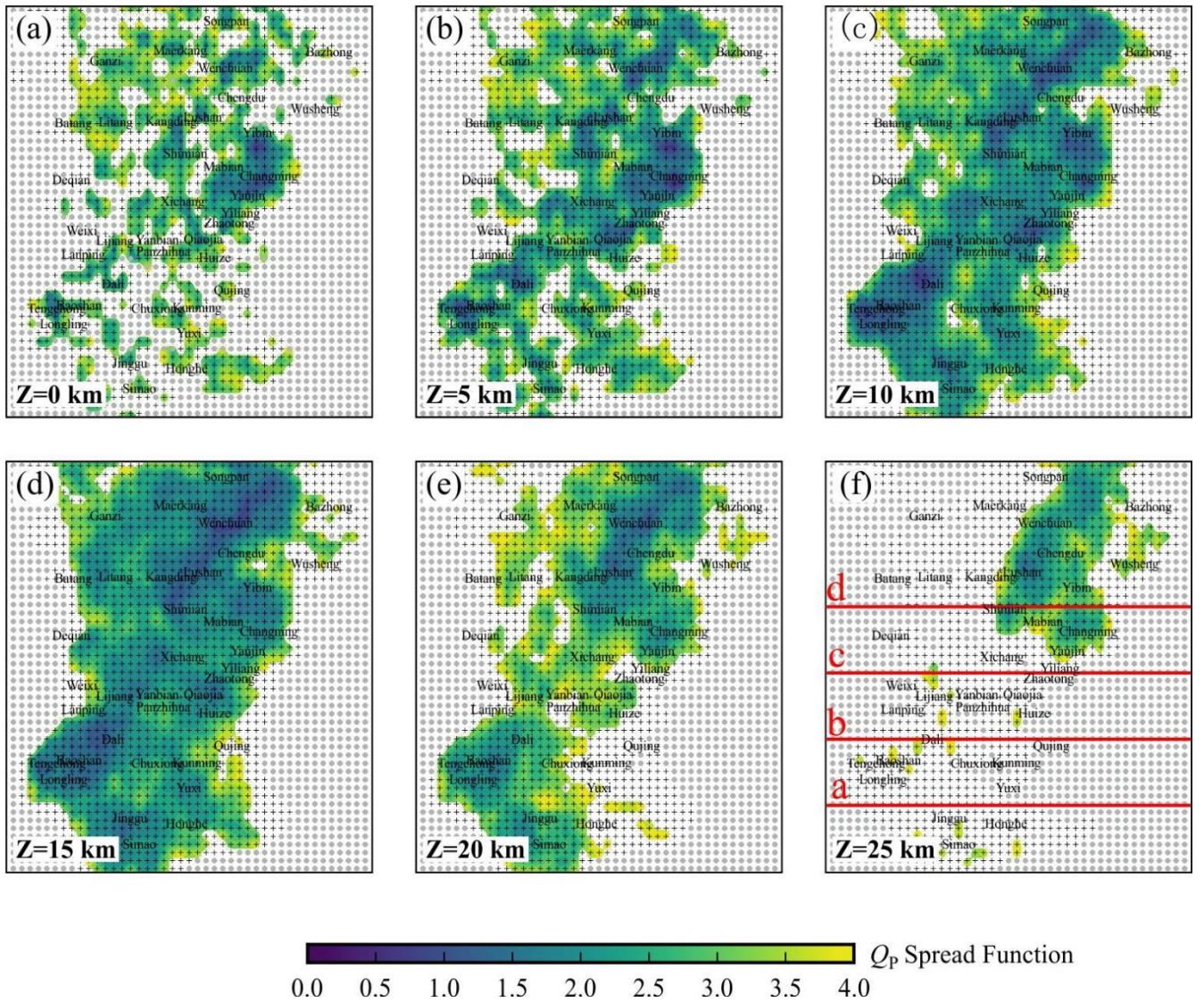
Figure 6: The spread function distribution of layered Q_P model (SF < 4).

The black plus sign represents the grid points, and the gray filled circle represents the grid that does not participate in the inversion. (f) The red solid line corresponds to each profile in Figure 5, and the letters above correspond to the numbers in Figure 7.
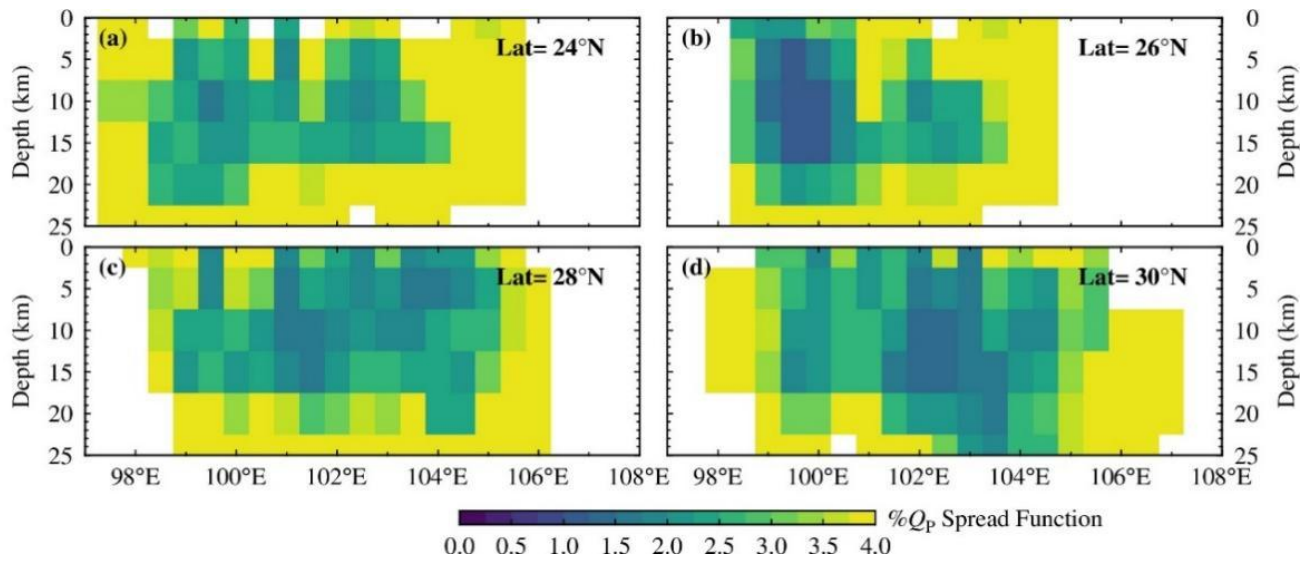
Figure 7: The spread function distribution of the Q_P model along different latitudes.

3.3 3D Q_P model in the CSES

The layered Q_P model (Fig. 8) shows that the attenuation structure of CSES exhibits significant lateral heterogeneity. Along
215 the main fault zones at depths of 0 km and 5 km are dominated by low Q_P values (high attenuation), and there are high Q_P anomalies (low attenuation) in the Songpan-Ganzi block (SPGZB) and the Chuan-Dian block (CDB). Hot springs are developed along the main fault zones (Fig. 8a), which correspond well with the shallow high attenuation anomalies, indicating that the shallow layers of the main fault zones are rich in fluids. The study area at a depth of 10 km is mainly characterized by high Q_P anomalies, while low Q_P anomalies are mainly distributed in the middle section of the Xiaojiang
220 fault (XJF) and the Simao basin. At a depth of 15 km, high Q_P anomalies are predominant, distributed in the NS direction, while low Q_P anomalies are mainly found in the Sichuan basin (SCB) and areas such as Qujing and Simao. At a depth of 20 km, low Q_P anomalies are predominant, while high Q_P anomalies are distributed on both sides of the Longmenshan fault zone. At a depth of 25 km, high Q_P anomalies still dominate along the Longmenshan fault zone.
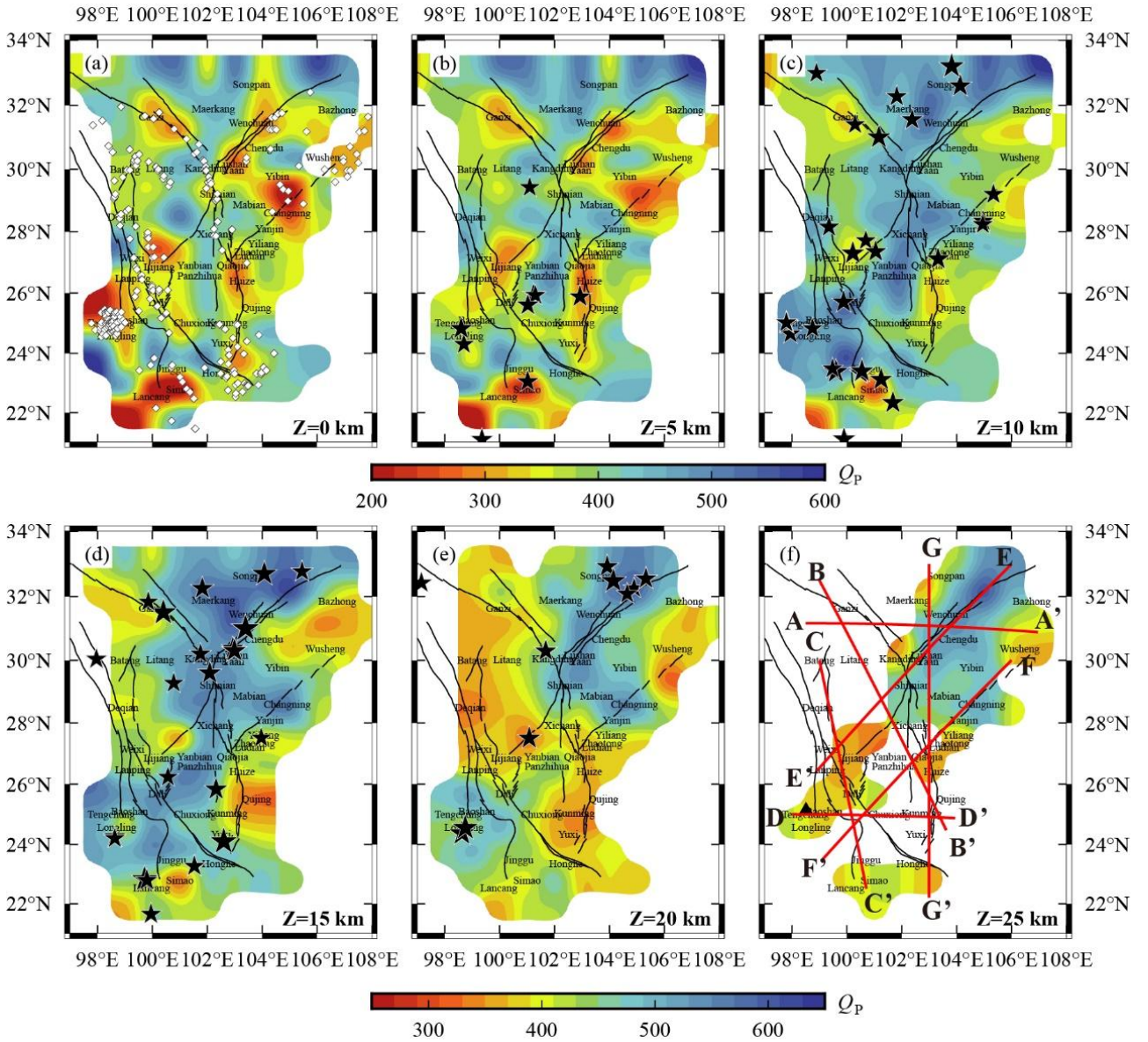
Figure 8: Layered Q_P model (SF < 4).

(a) White diamonds represent the distribution of hot springs (Zhang et al., 2021). (b)-(e) Black stars indicate earthquakes of magnitude 6 or greater since 1970 within a 2.5 km depth range for each. The size of the symbols is proportional to the magnitude of the earthquakes. (f) Red solid lines represent the profiles, with letters denoting the names of the profiles.

To better study the distribution characteristics of the medium structure in depth, we plot seven Q_P profiles (Fig. 8f). At the same time, the V_P model of SWChina CVM-1.0 and SWChina CVM-2.0 established by previous researchers are compared to facilitate the comprehensive analysis of velocity and attenuation structure. Both the previous two versions of V_P models and the Q_P model obtained in this paper generally exhibit low-value anomalies in the shallow layers and high-value anomalies in

the deep layers. However, there are significant differences in the patterns of Q_P anomalies obtained in this paper and V_P anomalies from previous studies. In basin areas such as Sichuan and Simao basins, the middle and upper crust exhibits obvious low Q_P anomalies (Figs. 9a, c). Within the CDB enclosed by multiple large active faults, both ends of NW and SE exhibit low Q_P characteristics throughout the upper and middle crust, while V_P shows low-value anomalies only within 10 km (Fig. 9b). Beneath some large fault zones, such as the Jinshajiang fault (JSJF), Longmenshan fault (LMSF), and XJF, there are obvious low Q_P anomalies in the entire upper and middle crust, with low V_P anomalies distributed at depths within 10 km (Figs. 9e, g). There are also some large fault zones, such as the Huayingshan fault (HYSF), Red River fault (RRF), Daliangshan fault (DLSF), and the southern end of the Zemuhe fault (ZMHF), with low V_P and low Q_P anomalies at depths within 10 km, and high V_P and high Q_P anomalies below 10 km (Figs. 9c, f, g). Notably, the bothe sides of the northern RRF and the junction of the southern segment of the RRF with the XJF, exhibit a clear low Q_P anomaly within 10 km (Figs. 9c, g). In the Tengchong volcanic area, the upper and middle crust exhibit a low Q_P anomaly that dips to the east (Fig. 9d), while V_P shows a low value anomaly only within 5 km. In addition, there are high Q_P anomalies below the Lancangjiang Fault (LCJF) (Figs. 9c, d), while Lianfeng fault (LFF) is mainly characterized by high V_P and high Q_P anomalies in the upper and middle crust (Fig. 9f). The southern section of the Anninghe Fault (ANHF) exhibits high Q_P anomalies (Figs. 9b, f). From the LMSF southward to the XJF, the upper crust shows high V_P and high Q_P anomalies (Fig. 9g). The differences in the distribution of low Q_P anomalies and low V_P anomalies in different regions obtained in this article indicate that the Q_P model obtained in this paper can supplement the physical properties of the medium not revealed by the V_P models. In the following, we will analyze and discuss the medium's properties and the seismogenic environment for moderate and strong earthquakes by integrating the characteristics of V_P and Q_P in CSES.
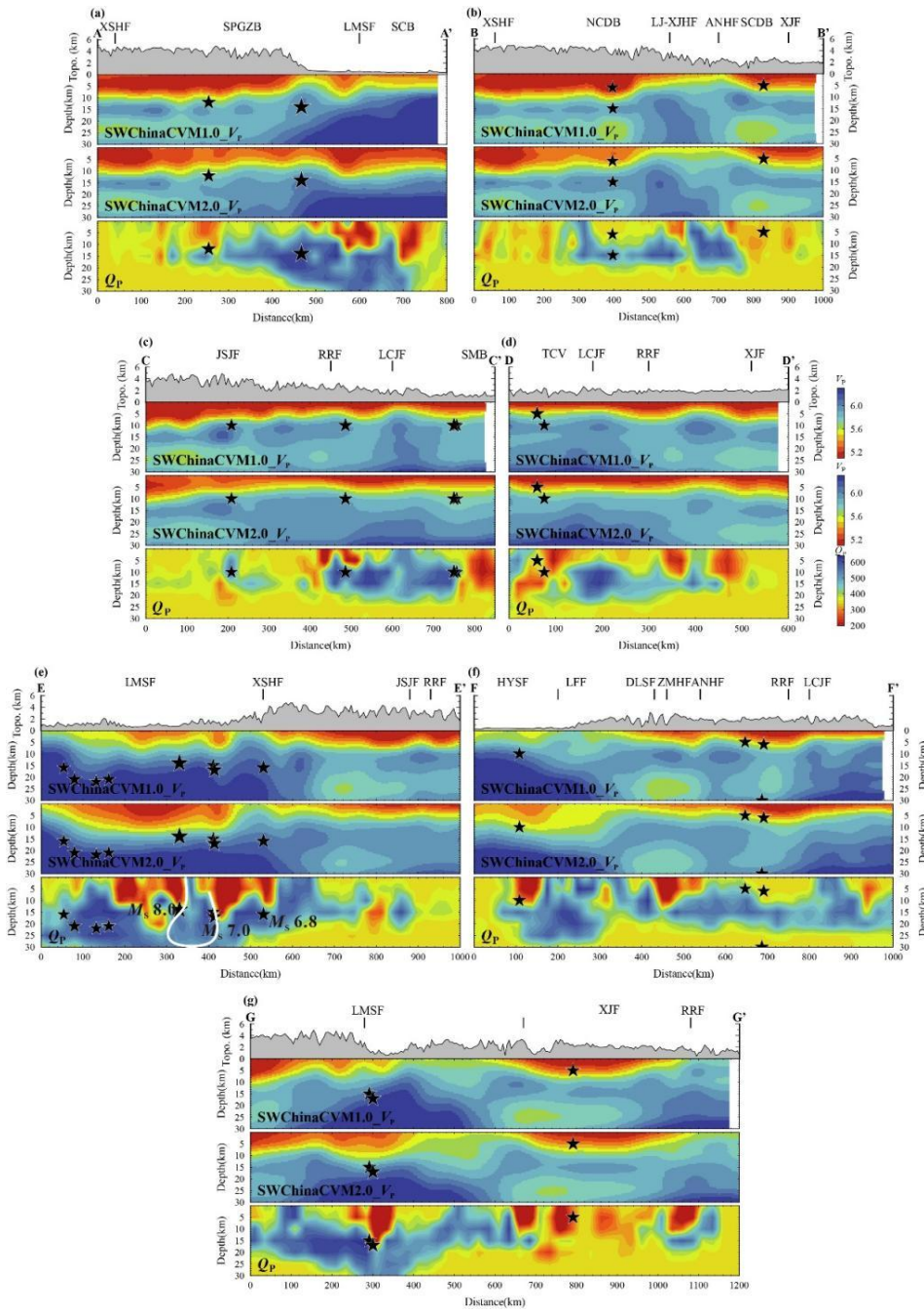
Figure 9: V_P and Q_P models of various profiles.

Each subplot from top to bottom represents the V_P results of SWChinaCVM1.0 and 2.0, and the Q_P results obtained in this paper. The black bar above the topographic map represents the position of the fault. Black stars represent earthquakes with M ≥ 6 within 25 km on both sides of the profile since 1970. The size of the symbols is proportional to the magnitude of the earthquakes. The white curve in (e) encloses the low-attenuation area between the 2008 Wenchuan M_S 8.0 earthquake and the 2013 Lushan M_S 7.0 earthquake. Other symbols are the same as in Figure 8.

4 Discussion

4.1 Spatial distribution characteristics of media structure in typical structural areas

The V_P models from SWChinaCVM-1.0 and SWChinaCVM-2.0 indicate, with the LMSF as the boundary, the depth of the low V_P anomaly in the SPGZB on the west side is greater than that to in the SCB on the east side (Fig. 9a). In contrast, the Q_P model shows that within 10 km of the shallow layer, the SPGZB exhibits low attenuation anomalies while the SCB shows high attenuation anomalies (Fig. 9a), which is consistent with the V_S model and the thickness of the sedimentary layers obtained by Yang et al. (2023), as well as the V_P and V_S models obtained by CSES-VM1.0. We believe that the distinct low V_P, low V_S, and low Q_P anomalies in the shallow layers of the SCB reflect the presence of several kilometers of Cenozoic-Mesozoic sedimentary rocks in the SCB.

The NW-trending BB' profile across the CDB reveals that the northwestern and southeastern segments of the CDB exhibit high attenuation characteristics in the upper and middle crust, while the central region is predominantly characterized by low attenuation features. The low attenuation feature between the Lijiang-Xiaojinhe fault (LJ-XJHF) and ANHF corresponds to the high velocity anomalies obtained by CSES-VM1.0 along the similar profile. The BB' profile crosses the inner zone of the Emeishan Large Igneous Province (ELIP), which is primarily composed of flood basalts, accompanied by mafic and felsic intrusive rocks (Ren et al., 2022). Various geophysical studies have indicated that the inner zone of the ELIP is a rigid region with high V_P, high V_S, high Poisson's ratio, high density, and high resistivity (Bao et al., 2015; Xu et al., 2015; Li et al., 2020; Zhang et al., 2020), which coincides with the high Q_P anomalies obtained in this study in the CDB. Therefore, the high Q_P anomalies reflect the basalt characteristics of the inner zone of the ELIP. At a depth of 20 km, the high attenuation anomalies of the CDB are connected near Xichang (Fig. 8e), which is similar to the 2 Hz Q_{Lg} model obtained by Zhou et al. (2008) in the Sichuan-Yunnan region. However, it differs from the Q_{Lg} model (0.2-2.0 Hz) in the Tibetan Plateau obtained by Zhao et al. (2013). Previous velocity models have also shown (Yao et al., 2008; Bao et al., 2015; Yang et al., 2020, 2023; Liu et al., 2021, 2023; Wu et al., 2024) that the low-velocity zone located in the northwestern CDB and the low-velocity zone along the Xiaojiang Fault are separated by the ELIP. Among them, the V_S model obtained by Yang et al. (2023) shows that in the middle and lower crust at a depth of 20-30 km, the low-velocity anomalies of the western Sichuan and the XJF are significantly separated by a high-velocity body, which extends continuously from the east side of the SCB, crosses the ANHF, and terminates at the central Yunnan block. Since the Q_P model obtained in this study in the CDB have no resolution below 20 km, it is not possible to determine the characteristics of Q_P in the middle and lower crust of the CDB, and it is not possible to accurately describe the distribution of flow in the middle and lower crust of the Tibetan Plateau.

Significant low-velocity and high-attenuation anomalies are observed in the shallow layers along LMSF (Fig. 9e), and the range of high attenuation anomalies is deeper. Between the LMSF and the XSHF, two distinct high-attenuation zones are present in the upper crust, corresponding to the 2008 Wenchuan M_S 8.0 earthquake and the 2013 Lushan M_S 7.0 earthquake source areas, respectively. The main rupture of the Wenchuan earthquake occurred near Yingxiu on the Beichuan Fault, with both the Beichuan Fault and the Pengguan Fault experiencing severe ruptures, with rupture lengths reaching 240–300 km

and ~90 km, respectively (Zhang et al., 2009a). These two major earthquakes have significantly fragmented the medium along the Longmenshan Fault. Additionally, a series of complex rock bodies (757–805 Ma) are exposed along the Longmenshan Fault from north to south, including the Nanba Complex, Pengguan Complex, Baoxing Complex, and Kangding Complex (Zhang et al., 2009b). Therefore, the high attenuation anomaly may partly reflect strong medium inhomogeneity, leading to scattering attenuation. The high-attenuation anomaly above the epicenter of the Wenchuan M_S 8.0 earthquake is consistent with the Q_P and Q_S models obtained by Zhou (2016) and the low-resistivity anomaly characteristics reported by Zhao et al. (2012). Zhao et al. (2012) suggested that the high-conductivity body beneath the LMSF in the Wenchuan earthquake source area may reflect an increase in fluid content. We believe that the two high-attenuation zones in the shallow layers of the LMSF indicate the presence of mechanically weak zones along the fault. Considering the development of hot springs along the LMSF, these mechanically weak zones are likely influenced by fluids in the upper crust. The occurrence of the Wenchuan M_S 8.0 earthquake and the Lushan M_S 7.0 earthquake may be related to the role of fluids.

The Xiaojiang fault (XJF) is the southeastern boundary of the CDB, extends over 400 km from north of Qiaojia to southeast of Jianshui. The fault zone is situated in a high heat flow area of 85 mW/m2 (Yuan et al., 2006), along which more than 20 basins with different scales, and hot springs are developed. The north-south trending GG' profile reveals (Fig. 9g) that the entire upper and middle crust along the XJF is dominated by significant low Q_P anomalies, which terminate at the southern end of the Red River fault (RRF). These low Q_P anomalies are in good agreement with the Q_{Lg} models at different frequencies (Zhou et al., 2008; Zhao et al., 2013) and the Q_P model obtained by previous studies (Dai et al., 2020). The resolution of the Q_P model along the XJF in this study is superior to that of Dai et al. (2020) at depths of 5 km and 15 km. The low Q_P anomalies obtained in this study also show good consistency with the low V_P anomalies reported by previous studies (Wu et al., 2013, 2024). The electrical resistivity structure along the similar profile shows an alternating pattern of high and low anomalies (Yu et al., 2022), and the low resistivity anomalies in the upper and middle crust may reflect the presence of saline fluids and highly conductive minerals. Geochemical studies also indicate that the XJF is dominated by crustal heat flow (Zhang et al., 2021). Therefore, the low-velocity and high-attenuation anomalies in the upper and middle crust of the XJF reflect abundant fluids in the fault zone. The prominent high-attenuation anomalies are concentrated at the northern and southern ends of the XJF. Geochemical research also shows that the relatively high temperatures and ion concentrations of hot spring water, as well as the relatively high fluxes of soil gas radon and carbon dioxide, are concentrated in the northern and southern segments of the XJF, which corresponds to the spatial distribution of seismicity and fault slip rates (He et al., 2023). Shi and Wang (2017) shows that the permeability is higher in the northern and southern segments of the XJF. In summary, we suggest that the low-velocity, low-resistivity, and high-attenuation anomalies in the upper crust of the XJF reflect the presence of fluids and highly conductive minerals beneath the fault zone. Intense fault activity in the southern and northern segments leads to high degree of crustal medium fragmentation, which may also enhance permeability and accelerate the water-rock interaction and soil gas emission within the fault zone. XJF has experienced multiple tectonic movements, with acidic and basic magmatic intrusions during the Jinning, Caledonian, and Hercynian periods, causing large

amounts of basalt and ultrabasic rock bodies to be exposed along the fault (Li, 1993). The high attenuation observed along the fault may also be due to scattering attenuation caused by the inhomogeneity of these unconsolidated rocks.

4.2 Low Q_P anomaly in the Western Yunnan region

The CC' profile along the Jinsha River fault (JSJF) shows that (Fig. 9c) the fault is predominantly characterized by low Q_P
330   anomalies, and high Q_P anomalies are dominant in the south of the Red River fault (RRF). Zhou et al. (2020) found that the He in the hot spring gases in the JSJF-RRF is mainly from the crust, and the high values of H2 concentration and He isotopic ratios appear at three fracture junctions of the JSJF with the Batang fault, the Zhongdian fault with the RRF, and the southern section of RRF with the XJF, respectively, which has a good corresponding relationship with the high attenuation anomalies obtained in different depths in this paper, especially in the intersection area of Zhongdian fault and RRF (Fig. 9c) and the
335   intersection area of the southern section of RRF and XJF (Fig. 9g). The Simao basin exhibits low Q_P anomalies. It is a Mesozoic Cenozoic sedimentary basin, mainly composed of mudstone and sandstone. There are many hot springs and salt springs in the basin. The obvious high attenuation anomalies in the basin reflect that it being fluid- rich in the upper crust.

The Tengchong volcano (TCV), located in the southeastern Tibet Plateau, is one of the largest active volcanoes in China (Fig. 1a). TCV is characterized by a large amount of magmatic gas (carbon dioxide and sulfide) emissions (Zhao et al., 2011,
340   2012), active hydrothermal cycle (Jiang et al., 2019), high surface heat flow ($\geq$ 90 mW/m2), and strong earthquakes during the Holocene (Zhao et al., 2020) and volcanic activity (Wang et al., 2007; Zou et al., 2014). The measurement of hot spring fluids also shows that there are a large number of hot spring fluids in the TCV (Fig. 8a), indicating that the TCV is rich in thermal materials and fluids. Previous inversion of the crust beneath Tengchong volcano yielded low V_S anomalies (Shen et al., 2022; Yang et al., 2023; Lin et al., 2024). The DD' profile across the TCV shows a high-attenuation anomaly that dips to
345   the west beneath the TCV (Fig. 9d). Zhao et al. (2021) found the low V_S anomaly at the depth of 20-35 km to the west of the TCV, which revealed a large basaltic magma reservoir and the melt fraction of 2% -4.5%. The high attenuation anomaly obtained in the middle and upper crust of TCV in this paper is likely connected to the low V_S anomaly obtained in the middle and lower crust by previous researchers. The westard- dipping high attenuation anomaly in the upper and middle crust of the TCV depicts the possible upwelling of deep magma from west to east, which is also a direct reflection of partial melting and
350   fluids.

4.3 Seismogenic Mechanism of Moderate and Strong Earthquakes

Most of the historical earthquakes in Fig. 1 lacked depth information before 1970. Therefore, we only consider the relationship between earthquakes with M $\geq$ 6 and the Q_P model in CSES after 1970. Some studies have found that large crustal earthquakes often occur in high-velocity anomaly areas (Liu et al., 2023; Huang and Zhao, 2004; Pei et al., 2019; Sun
355   et al., 2021). They believe that the high-velocity anomaly area may be the asperity of the fault, with high stress accumulation, resulting in large earthquakes. Other studies have found that moderate and strong earthquakes with M $\geq$ 6 often occur in high attenuation areas or at the boundaries of high and low attenuation (Zhou et al., 2008; Pei et al., 2009; Liu

and Zhao, 2015; Zhou et al., 2020). These results support that fluids increase the pore pressure of faults and promote earthquake nucleation. In this paper, the earthquakes within 2.5 km of each depth layer are projected onto the layered Q_P model, and the earthquakes with M ≥ 6 within 25 km on both sides of each profile are projected onto the Q_P model (Figs. 8, 9). The results show that, compared with the velocity models, the relationship between earthquakes above M 6 and the attenuation model is closer (Fig. 9). Earthquakes with M ≥ 6 in western Yunnan are distributed in the low-attenuation area and the boundary of high and low attenuation anomalies (Fig. 9c). Two major earthquakes in TVC occurred in the high attenuation area (Fig. 9d). Earthquakes with M ≥ 6 along the northeastern segment of the Longmenshan fault (LMSF) are aftershocks of the 2008 Wenchuan M_S 8.0 earthquake, which all occurred in the low attenuation area or the boundary of high and low attenuation (Fig. 9e). The major earthquakes in southwest section of the LMSF are 2008 Wenchuan M_S 8.0 earthquake, 2013 Lushan M_S 7.0 earthquake, 2022 Lushan M_S 6.1 earthquake and Luding M_S 6.8 earthquake from northeast to southwest, which all occurred at the boundary of high-low attenuation anomalies or low attenuation area (Figs. 9e, g), similar to the V_P imaging results obtained by previous studies (Li et al., 2013; Pei et al., 2014; Liu et al., 2023). Earthquakes with M ≥ 6 along the Huayingshan fault occurred at the boundary of high and low attenuation (Fig. 9f). Our result shows that earthquakes with M ≥ 6 in CSES generally occur in the low attenuation area or the boundary area of high and low attenuation anomalies. The low attenuation zone may represent the asperity with high mechanical strength, which is conducive to stress accumulation. The boundary of high and low attenuation anomalies corresponds to the gradient zone of stress change, which is more prone to sudden change in stress. Both cases promote the rupture of faults and trigger large earthquakes.

Our result also shows that the source area of the Lushan earthquake and the Wenchuan earthquake are separated by a low attenuation zone (Fig. 9e). The results of body wave velocity imaging showed that the Wenchuan-Lushan seismic gap is located in the low-velocity anomaly area (Li et al., 2013; Pei et al., 2014). They believed that the intensity of this area is low and not enough to generate strong earthquakes. Wang et al. (2015) observed an obvious seismic moment deficit in the seismic gap through GPS velocity data, suggesting its potential to host strong earthquakes. Wang et al. (2018) found that the microseismic activity in the seismic gap is relatively weak compare to the north and south sides, indicating that the possibility of accumulated stress and strain being released through microseisms is very small. Diao et al. (2018) studied the post earthquake mechanism of the Wenchuan earthquake and found that there is almost no afterslip distribution in the gap, and it is still accumulating strain through GPS observation, suggesting that the gap has a relatively large seismic risk. In addition, based on the study of Coulomb stress, it was found that the Wenchuan earthquake and Lushan earthquake have greatly enhanced the stress in the gap, thus greatly increasing the possibility of strong earthquakes (Guo et al., 2020). The low attenuation anomaly region in the seismic gap between the two strong earthquake obtained by this paper suggests that the medium strength in this region is high and is still in the stress accumulation. Contrary to the low-velocity characteristics, it is consistent with the observation results of GPS. Therefore, we support that the seismic gap poses a danger of major earthquakes in the future.

5 Conclusions

In this study, we collect and sort out the earthquake catalog, phase reports and seismic waveforms of magnitude 1.5 or above recorded by 582 stations in the China Seismic Experimental Site from 2013 to 2023. Through seismic clustering and phase quality control, we select 35, 778 high-quality seismic waveforms. The high resolution 3D Q_P model of CSES is obtained by using SIMUL2000 program. The horizontal resolution of the model is 50 km and the vertical resolution is 5 km. Combined with other geophysical inversion results, geochemical observation and geological structure data, this paper has the following understanding of the medium environment of the middle and upper crust of CSES:

(1) In the depth of 5 km along the large fault zone in the Chuan-Dian region, the Q_P model exhibits low-value anomalies, which corresponds well with the characteristics of hot spring development around the fault zone, reflecting the strong tectonic movement of major active fault zones leading to a highly fragmented and fluid-rich shallow medium. The Q_P model in the upper and middle crust of Sichuan Basin and Simao basin also shows low-value anomalies, reflecting the characteristics of thicker sedimentary layers in these areas.

(2) The high attenuation anomalies obtained in the upper and middle crust of Tengchong volcano is likely to be connected with the low V_S anomaly in the middle and lower crust. The westward-dipping high attenuation anomalies in the upper and middle crust depict the upwelling the pattern of magma uprising from west to east.

(3) There are two obvious high attenuation anomaly areas under the Longmenshan fault, which are located above the epicenter of the 2008 Wenchuan M_S 8.0 earthquake and 2013 Lushan M_S 7.0 earthquake, respectively. The fluids in the upper crust may promote the nucleation of the two large earthquakes. The two seismic source areas are separated by a low attenuation area, which may has high stress accumulation and still have the risk of large earthquakes in the future.

(4) The Xiaojiang fault shows high attenuation anomalies in the middle and upper crust, and the anomalies at the north and south ends are more obvious. The high attenuation anomaly at the intersection of the southern end and the Red River fault corresponds well to the high H2 and He isotopic content in hot springs, indicating that the Xiaojiang fault is rich in fluid and high conductivity minerals in upper and middle crust. The strong fault activity in the southern and northern segments leads to high degree of crustal media fragmentation and enhances the permeability of the fault zone.

(5) Most moderate and strong earthquakes with M ≥ 6 in CSES occur in the low attenuation areas or the boundary area of high-low attenuation anomalies, which is similar to the spatial relationship between earthquakes and velocity anomalies. This paper considers that such an abnormal area is conducive to stress accumulation and sudden change in stress, which is prone to large earthquakes.

Code/Data Availability

The earthquake catalogues, phase reports are provided by China Earthquake Networks Center, National Earthquake Data Center (CENC, 2021), Sichuan Earthquake Administration and Yunnan Earthquake Administration. The inverted 3D Q_P models are available at doi: 10.5281/zenodo.13994425. The version v1 of the Simul2000 program used for 3D seismic

tomography is preserved at doi:10.5281/zenodo.5547888, available via Thurber & Eberhart-Phillips (2021). All figures are made with the Generic Mapping Tools Version 6 (Wessel et al., 2019) and CorelDRAW 2020 (Copyright © 2020 Corel
425 Corporation) from https://www. corel.com/.

Competing Interests

The authors acknowledge that there are no conflicts of interest.

Acknowledgements

We extend our sincere gratitude to Shaolin liu and another anonymous reviewer for their valuable comments and suggestions.
430 This study was jointly funded by the National Key R&D Program (2021YFC3000704), the National Natural Science Foundation of China (42174066) and the Central Public-interest Scientific Institution Basal Research Fund (CEAIEF20240405). Most of figures in this paper were plotted by GMT 6 software (Wessel et al., 2019).

Author Contribution

Lianqing Zhou wrote, reviewed and edited the manuscript.
435 Mengqiao Duan wrote the original manuscript.
Ying Fu provided data for Sichuan Province.
Yanru An supplemented the data for Sichuan and Yunnan provinces.
Jingqiong Yang provided data for Yunnan Province.
Lianqing Zhou and Xiaodong Zhang provided project funding for this research.

440 **References**

Bai, D., Unsworth, M. J., Meju, M. A., Ma, X., Teng, J., Kong, X., Sun, Y., Sun, J., Wang, L., Jiang, C., Zhao, C., Xiao, P., and Liu, M.: Crustal deformation of the eastern Tibetan plateau revealed by magnetotelluric imaging, Nat. Geosci., 3, 358–362, https://doi.org/10.1038/ngeo830, 2010.

Bao, X., Sun, X., Xu, M., Eaton, D. W., Song, X., Wang, L., Ding, Z., Mi, N., Li, H., Yu, D., Huang, Z., and Wang, P.: Two
445 crustal low-velocity channels beneath SE Tibet revealed by joint inversion of Rayleigh wave dispersion and receiver functions, Earth Planet. Sci. Lett., 415, 16–24, https://doi.org/10.1016/j.epsl.2015.01.020, 2015.

Bao, X., Song, X., Eaton, D. W., Xu, Y., and Chen, H.: Episodic Lithospheric Deformation in Eastern Tibet Inferred From Seismic Anisotropy, Geophys. Res. Lett., 47, e2019GL085721, https://doi.org/10.1029/2019GL085721, 2020.

Brune, J. N.: Tectonic stress and the spectra of seismic shear waves from earthquakes, J. Geophys. Res., 75, 4997–5009, https://doi.org/10.1029/JB075i026p04997, 1970.

Chen, Y., Gu, Y. J., Mohammed, F., Wang, J., Sacchi, M. D., Wang, R., and Nguyen, B.: Crustal attenuation beneath western North America: Implications for slab subduction, terrane accretion and arc magmatism of the Cascades, Earth Planet. Sci. Lett., 560, 116783, https://doi.org/10.1016/j.epsl.2021.116783, 2021.

Dai, A., Tang, C.-C., Liu, L., and Xu, R.: Seismic attenuation tomography in southwestern China: Insight into the evolution of crustal flow in the Tibetan Plateau, Tectonophysics, 792, 228589, https://doi.org/10.1016/j.tecto.2020.228589, 2020.

Deng, Y., Byrnes, J. S., and Bezada, M.: New Insights Into the Heterogeneity of the Lithosphere-Asthenosphere System Beneath South China From Teleseismic Body-Wave Attenuation, Geophys. Res. Lett., 48, https://doi.org/10.1029/2020GL091654, 2021.

Diao, F., Wang, R., Wang, Y., Xiong, X., and Walter, T. R.: Fault behavior and lower crustal rheology inferred from the first seven years of postseismic GPS data after the 2008 Wenchuan earthquake, Earth Planet. Sci. Lett., 495, 202–212, https://doi.org/10.1016/j.epsl.2018.05.020, 2018.

Duan, M., Zhou, L., Zhao, C., Liu, Z., and Zhang, X.: High-Resolution 3D QP and QS Models of the Middle Eastern Boundary of the Sichuan–Yunnan Rhombic Block: New Insight into Implication for Seismogenesis, Seismol. Res. Lett., https://doi.org/10.1785/0220230232, 2024.

Eberhart-Phillips, D.: Three-dimensional velocity structure in northern California Coast Ranges from inversion of local earthquake arrival times, Bull. Seismol. Soc. Am., 76, 1025–1052, 1986.

Eberhart-Phillips, D. and Chadwick, M.: Three-dimensional attenuation model of the shallow Hikurangi subduction zone in the Raukumara Peninsula, New Zealand, J. Geophys. Res., 107, 2033–2050, https://doi.org/10.1029/2000JB000046, 2002.

Eberhart-Phillips, D. and Michael, A. J.: Seismotectonics of the Loma Prieta, California, region determined from three-dimensional Vp, Vp/Vs and seismicity, J. Geophys. Res., 103, 21099–21120, https://doi.org/10.1029/98JB01984, 1998.

Eberhart-Phillips, D., Chadwick, M., and Bannister, S.: Three-dimensional attenuation structure of central and southern South Island, New Zealand, from local earthquakes, J. Geophys. Res., 113, B05308–B05308, https://doi.org/10.1029/2007JB005359, 2008.

Evans, J. R., Eberhart-Phillips, D., and Thurber, C.: User's manual for SIMULPS12 for imaging Vp and Vp/Vs : A derivative of the "Thurber" tomographic inversion SIMUL3 for local earthquakes and explosions, 1994.

Fu, Y. V., Gao, Y., Li, A., Li, L., and Chen, A.: Lithospheric structure of the southeastern margin of the Tibetan Plateau from Rayleigh wave tomography: Lithospheric Velocity Structure of SE Tibet, J. Geophys. Res., 122, 4631–4644, https://doi.org/10.1002/2016JB013096, 2017.

Guo, H. and Thurber, C.: Temporal Changes in Seismic Velocity and Attenuation at The Geysers Geothermal Field, California, From Double-Difference Tomography, J. Geophys. Res., 127, e2021JB022938, https://doi.org/10.1029/2021JB022938, 2022.

Han, S., H. Zhang, H. Xin, W. Shen, and H. Yao: USTClitho2.0: Updated Unified Seismic Tomography Models for Continental China Lithosphere from Joint Inversion of Body-Wave Arrival Times and Surface-Wave Dispersion Data, Seismol. Res. Lett. 93, no. 1, 201–215, doi: 10.1785/0220210122, 2022.

Hauksson, E., and P. M. Shearer: Attenuation models (Qp and Qs) in three dimensions of the southern California crust : Inferred fluid saturation at seismogenic depths, J. Geophys. Res. 111, no. B5, B05302–B05322, doi: 10.1029/2005JB003947, 2006.

He, H., Chen, Z., Liu, Z., Gao, Z., Hu, L., Lu, C., Shao, J., and Li, Y.: Geochemical features of fluid in Xiaojiang fault zone, Southeastern Tibetan plateau: Implications for fault activity, Appl. Geochem., 148, 105507, https://doi.org/10.1016/j.apgeochem.2022.105507, 2023.

Hu, S., He, L., and Wang, J.: Heat £ow in the continental area of China: a new data set, Earth Planet. Sci. Lett., 179, 407–419, 2000.

Huang, Z., Wang, L., Xu, M., and Zhao, D.: P Wave Anisotropic Tomography of the SE Tibetan Plateau: Evidence for the Crustal and Upper-Mantle Deformations, J. Geophys. Res., 123, 8957–8978, https://doi.org/10.1029/2018JB016048, 2018.

Jiang, G., Hu, S., Shi, Y., Zhang, C., Wang, Z., and Hu, D.: Terrestrial heat flow of continental China: Updated dataset and tectonic implications, Tectonophysics, 753, 36–48, https://doi.org/10.1016/j.tecto.2019.01.006, 2019.

Karato, S., and H. A. Spetzler: Defect microdynamics in minerals and solid-state mechanisms of seismic wave attenuation and velocity dispersion in the mantle, Rev. Geophys., 28, 399 – 421, 1990.

Lees, J. M., and G. T. Lindley: Three-dimensional attenuation tomography at Loma Prieta: Inversion of t* for Q, J. Geophys. Res. 99, no. B4, 6843–6863, doi: 10.1029/93JB03460, 1994.

Li, P. The Xianshuihe-Xiaojiang fault zone: Part I: Regional Tectonic Background, Seismological Press, Beijing (in Chinese), 284pp., ISBN7-5028-0987-2/P·607, 1993.

Li, X., Bai, D., Ma, X., Chen, Y., Varentsov, I. M., Xue, G., Xue, S., and Lozovsky, I.: Electrical resistivity structure of the Xiaojiang strike-slip fault system (SW China) and its tectonic implications, J. Asian Earth Sci., 176, 57–67, https://doi.org/10.1016/j.jseaes.2019.01.031, 2019.

Li, X., Ma, X., Chen, Y., Xue, S., Varentsov, I. M., and Bai, D.: A plume-modified lithospheric barrier to the southeastward flow of partially molten Tibetan crust inferred from magnetotelluric data, Earth Planet. Sci. Lett., 548, 116493, https://doi.org/10.1016/j.epsl.2020.116493, 2020.

Li, Z., Tian, B., Liu, S., and Yang, J.: Asperity of the 2013 Lushan earthquake in the eastern margin of Tibetan Plateau from seismic tomography and aftershock relocation, Geophys. J. Int., 195, 2016–2022, https://doi.org/10.1093/gji/ggt370, 2013.

Lin, G.: Three-dimensional compressional wave attenuation tomography for the crust and uppermost mantle of Northern and central California, J. Geophys. Res., 119, 3462–3477, https://doi.org/10.1002/2013JB010621, 2014.

Lin, Y., Liu, S., Dinghui, Y., Xiwei, X., Shuxin, Y., and Wenshuai, W.: A multiscale magma system beneath the Tengchong volcano in western Yunnan revealed by ambient noise tomography, Geophys. J. Int., 1828–1839, 2024.

Liu, H., Pei, S., Liu, W., Xue, X., Li, J., Hua, Q., and Li, L.: Crustal and Upper Mantle Attenuation Structure Beneath the Southeastern Tibetan Plateau and Its Implications on Plateau Outgrowth, J. Geophys. Res. 129, no. 2, e2023JB026977, doi: 10.1029/2023JB026977, 2024.

Liu, X. and Zhao, D.: Seismic attenuation tomography of the Southwest Japan arc: new insight into subduction dynamics, Geophys. J. Int., 201, 135–156, https://doi.org/10.1093/gji/ggv007, 2015.

Liu, X., and D. Zhao: Seismic attenuation tomography of the Southwest Japan arc: new insight into subduction dynamics, Geophys. J. Int. 201, no. 1, 135–156, doi: 10.1093/gji/ggv007, 2015.

Liu, Y., Yao, H., Zhang, H., and Fang, H.: The Community Velocity Model V.1.0 of Southwest China, Constructed from Joint Body- and Surface-Wave Travel-Time Tomography, Seismol. Res. Lett., https://doi.org/10.1785/0220200318, 2021.

Liu Y., Yu Z., Zhang Z., Yao H., Wang W., Zhang H., Fang H., and Fang L.: The high-resolution community velocity model V2.0 of southwest China, constructed by joint body and surface wave tomography of data recorded at temporary dense arrays, Sci. China Earth Sci., https://doi.org/10.1007/s11430-022-1161-7, 2023.

McNamara, D. E.: Frequency dependent Lg attenuation in southcentral Alaska, Geophys. Res. Lett., 27(23), 3949 – 3952, 2000.

Pei, S., Cui, Z., Sun, Y., Toksoz, M. N., Rowe, C. A., Gao, X., Zhao, J., Liu, H., He, J., and Morgan, F. D.: Structure of the Upper Crust in Japan from S-Wave Attenuation Tomography, Bull. Seismol. Soc. Am., 99, 428–434, https://doi.org/10.1785/0120080029, 2009.

Pei, S., Zhang, H., Su, J., and Cui, Z.: Ductile Gap between the Wenchuan and Lushan Earthquakes Revealed from the Two-dimensional Pg Seismic Tomography, Sci. Rep., 4, 6489, https://doi.org/10.1038/srep06489, 2014.

Qiao, L., Yao, H., Lai, Y.-C., Huang, B.-S., and Zhang, P.: Crustal Structure of Southwest China and Northern Vietnam From Ambient Noise Tomography: Implication for the Large-Scale Material Transport Model in SE Tibet, Tectonics, 37, 1492–1506, https://doi.org/10.1029/2018TC004957, 2018.

Reyners, M., D. Eberhart-Phillips, G. Stuart: A three-dimensional image of shallow subduction: crustal structure of the Raukumara Peninsula, New Zealand. Geophys. J. Int. 137, 873–890. https://doi.org/10.1046/j.1365-246x.1999.00842.x, 1999.

Ren, Y., Lu, Z. W., Zhang, X., Xue, S., Wang, G.: Crustal structure of the Emeishan large igneous province inner zone revealed by deep seismic reflection profile. Chinese J. Geophys. (in Chinese), 65(2): 484-494, doi:10.6038/cjg2022P0196, 2022.

Shen, W., Ritzwoller, M. H., Kang, D., Kim, Y., Lin, F.-C., Ning, J., Wang, W., Zheng, Y., and Zhou, L.: A seismic reference model for the crust and uppermost mantle beneath China from surface wave dispersion, Geophys. J. Int., 206, 954–979, https://doi.org/10.1093/gji/ggw175, 2016.

550 Shen, W., Liu, S., Yang, D., Wang, W., Xu, X., and Yang, S.: The crustal and uppermost mantle dynamics of the Tengchong–Baoshan region revealed by P -wave velocity and azimuthal anisotropic tomography, Geophys. J. Int., 230, 1092–1105, https://doi.org/10.1093/gji/ggac105, 2022.

Shi, Z. and Wang, G.: Evaluation of the permeability properties of the Xiaojiang Fault Zone using hot springs and water wells, Geophys. J. Int., 209, 1526–1533, https://doi.org/10.1093/gji/ggx113, 2017.

555 Stachnik, J. C., G. A. Abers, and D. H. Christensen: Seismic attenuation and mantle wedge temperatures in the Alaska subduction zone, J. Geophys. Res. 109, no. B10304, doi: 10.1029/2004JB003018, 2004.

Sun, Q., Pei, S., Cui, Z., Chen, Y. J., Liu, Y., Xue, X., Li, J., Li, L., and Zuo, H.: Structure-controlled asperities of the 1920 Haiyuan M8.5 and 1927 Gulang M8 earthquakes, NE Tibet, China, revealed by high-resolution seismic tomography, Sci. Rep., 11, 5090, https://doi.org/10.1038/s41598-021-84642-7, 2021.

560 Tang, Z., Yang, D., Pan, W., Dong, X., Wang, N., and Xia, J.: Adjoint Attenuation Tomography of Sichuan–Yunnan Region, Seismol. Res. Lett., 94, 898–912, https://doi.org/10.1785/0220220189, 2023.

Thurber, C. H.: Local earthquake tomography: velocities and Vp/Vs-theory, Phys. Earth Planet. Inter., 75, 55–62, 1993.

Toomey, D. R., and G. R. Foulger: Tomographic inversion of local earthquake data from the Hengill-Grensdalur Central Volcano Complex, Iceland, J. Geophys. Res. 94, no. B12, 17497–17510, doi: 10.1029/JB094iB12p17497, 1989.

565 Wang, C., Liang, C., Deng, K., Huang, Y., and Zhou, L.: Spatiotemporal Distribution of Microearthquakes and Implications Around the Seismic Gap Between the Wenchuan and Lushan Earthquakes, Tectonics, 37, 2695–2709, https://doi.org/10.1029/2018TC005000, 2018.

Wang, Q., and Y. Gao: Rayleigh wave phase velocity tomography and strong earthquake activity on the southeastern front of the Tibetan Plateau, Sci. China Earth Sci. 57, no. 10, 2532–2542, doi: 10.1007/s11430-014-4908-2. 2014.

570 Wang, C., C. Liang, K. Deng, Y. Huang, and L. Zhou: Spatiotemporal Distribution of Microearthquakes and Implications Around the Seismic Gap Between the Wenchuan and Lushan Earthquakes, Tectonics 37, no. 8, 2695–2709, doi: 10.1029/2018TC005000, 2018.

Wang, F., Wang, M., Wang, Y., and Shen, Z.-K.: Earthquake potential of the Sichuan-Yunnan region, western China, J. Asian Earth Sci., 107, 232–243, https://doi.org/10.1016/j.jseaes.2015.04.041, 2015.

575 Wang, Y., Zhang, X., Jiang, C., Wei, H., and Wan, J.: Tectonic controls on the late Miocene–Holocene volcanic eruptions of the Tengchong volcanic field along the southeastern margin of the Tibetan plateau, J. Asian Earth Sci., 30, 375–389, https://doi.org/10.1016/j.jseaes.2006.11.005, 2007.

Wang, Z., Zhao, D., Liu, X., Chen, C., and Li, X.: P and S wave attenuation tomography of the Japan subduction zone, Geochem. Geophys. Geosystems, 18, 1688–1710, https://doi.org/10.1002/2017gc006800, 2017.

580 Wei, Z., and Zhao, L.: Lg-Q model for Sichuan and Yunnan region, Earth Planet. Phys., 3, 1–11, https://doi.org/10.26464/epp2019054, 2019.

Wu, J., Cai, Y., Wang, wei, Wang, weilai, Wang, C., Fang, L., Liu, Y., and Liu, J.: Three dimensional velocity model and its tectonic implications at China Seismic Experimental Site, eastern margin of the Tibetan Plateau, Sci. China Earth Sci., 54, 2304–2326, 2024.

585 Wu, J. P., Yang, T., Wang, W. L., Ming, Y. H., and Zhang, T. Z.: Three dimensional P-wave velocity structure around Xiaojiang fault system and its tectonic implications., Chin J Geophys Chin. Engl. Abstr., 56, 2257–2267, 2013.

Xin, H., H. Zhang, M. Kang, R. He, L. Gao, and J. Gao: High-Resolution Lithospheric Velocity Structure of Continental China by Double-Difference Seismic Travel-Time Tomography, Seismol. Res. Lett. 90, no. 1, 229–241, doi: 10.1785/0220180209, 2019.

590 Xu, T., Zhang, Z., Liu, B., Chen, Y., Zhang, M., Tian, X., Xu, Y., and Teng, J.: Crustal velocity structure in the Emeishan large igneous province and evidence of the Permian mantle plume activity, Sci. China Earth Sci., 58, 1133–1147, https://doi.org/10.1007/s11430-015-5094-6, 2015.

Yang, X., Luo, Y., Jiang, C., Yang, Y., Niu, F., and Li, G.: Crustal and Upper Mantle Velocity Structure of SE Tibet From Joint Inversion of Rayleigh Wave Phase Velocity and Teleseismic Body Wave Data, J. Geophys. Res., 128,
595 e2022JB026162, https://doi.org/10.1029/2022JB026162, 2023.

Yang, Y., Forsyth, D. W., and Weeraratne, D. S.: Seismic attenuation near the East Pacific Rise and the origin of the low-velocity zone, Earth Planet. Sci. Lett., 258, 260–268, https://doi.org/10.1016/j.epsl.2007.03.040, 2007.

Yang, Y., Yao, H., Wu, H., Zhang, P., and Wang, M.: A new crustal shear-velocity model in Southwest China from joint seismological inversion and its implications for regional crustal dynamics, Geophys. J. Int., ggz514,
600 https://doi.org/10.1093/gji/ggz514, 2019.

Yang, Y., Yao, H., Wu, H., Zhang, P., and Wang, M.: A new crustal shear-velocity model in Southwest China from joint seismological inversion and its implications for regional crustal dynamics, Geophys. J. Int., 1379–1393, https://doi.org/10.1093/gji/ggz514, 2020.

Yang, Y. J., Ritzwoller, M. H., Zheng, Y., Shen, W. S., Levshin, A. L., and Xie, Z. J.: A synoptic view of the distribution
605 and connectivity of the mid-crustal low velocity zone beneath Tibet, J. Geophys. Res. Solid Earth, 117, https://doi.org/10.1029/2011JB008810, 2012.

Yao, H., Beghein, C., and van der Hilst, R. D.: Surface wave array tomography in SE Tibet from ambient seismic noise and two-station analysis - II. Crustal and upper-mantle structure, Geophys. J. Int., 173, 205–219, https://doi.org/10.1111/j.1365-246X.2007.03696.x, 2008.

610 Yu, N., Wang, X., Li, D., Li, X., Wang, E., Kong, W., and Li, T.: The mechanism of deep material transport and seismogenic environment of the Xiaojiang fault system revealed by 3-D magnetotelluric study, Sci. China Earth Sci., 65, 1128–1145, https://doi.org/10.1007/s11430-021-9914-3, 2022.

Yuan, Y., Ma, Y., Hu, S., Guo, T., and Fu, X. (2006). Present day geothermal characteristics in South China. Chinese J. Geophys.(in Chinese), 49 (4): 1118-1126.

615 Zhang, M., Guo, Z., Xu, S., Barry, P. H., Sano, Y., Zhang, L., Halldórsson, S. A., Chen, A.-T., Cheng, Z., Liu, C.-Q., Li, S.-L., Lang, Y.-C., Zheng, G., Li, Z., Li, L., and Li, Y.: Linking deeply-sourced volatile emissions to plateau growth dynamics in southeastern Tibetan Plateau, Nat. Commun., 12, 4157, https://doi.org/10.1038/s41467-021-24415-y, 2021.

Zhang, P.,Deng, Q., Zhang, G., Ma, J., Gan, W., Min,W., Mao, F., and Wang, Q.. Strong earthquake activity and active blocks in China mainland. Sci. China Earth Sci. 46(Suppl.2), 13-24. https://doi.org/10.1360/03dz0002, 2003.

620 Zhang, Y., Feng, W. P., Xu, L. S., Zhou, C. H. and Chen, Y. T.: Spatio-temporal rupture process of the 2008 great Wenchuan earthquake, Sci. China Earth Sci., 52 (2):145-154. https://doi.org/10.1007/s11430-008-0148-7, 2009a.

Zhang. Z., Wang, Y., Chen, Y., Houseman, G. A., Tian, X. B., Wang, E., Teng, J. W.: Crustal structure across Longmenshan fault belt from passive source seismic profiling. Geophys. Res. Lett., 36, 2009b.

Zhang, Z., Yao, H., and Yang, Y.: Shear wave velocity structure of the crust and upper mantle in Southeastern Tibet and its
625   geodynamic implications, Sci. China Earth Sci., 63, 1278–1293, https://doi.org/10.1007/s11430-020-9625-3, 2020.

Zhao, C., Ran, H., and Chen, K. (2011). Present-day temperatures of magma chambers in the crust beneath Tengchong volcanic field, southwestern China: Estimation from carbon isotopic fractionation between CO2 and CH4 of free gases escaped from thermal springs. Acta Petrol. Sin., 27, 2883–2897.

Zhao, C., Ran, H., and Wang, Y. (2012). Present-day mantle-derived helium release in the Tengchong volcanic field,
630   Southwest China: Implications for tectonics and magmatism. Acta Petrol. Sin., 28, 1189–1204.

Zhao, G., Unsworth, M. J., Zhan, Y., Wang, L., Chen, X., Jones, A. G., Tang, J., Xiao, Q., Wang, J., Cai, J., Li, T., Wang, Y., and Zhang, J.: Crustal structure and rheology of the Longmenshan and Wenchuan Mw 7.9 earthquake epicentral area from magnetotelluric data, Geology, 40, 1139–1142, https://doi.org/10.1130/G33703.1, 2012.

Zhao, L. F., Xie, X. B., He, J. K., Tian, X. B., and Yao, Z. X.: Crustal flow pattern beneath the Tibetan Plateau constrained
635   by regional Lg-wave Q tomography, Earth Planet. Sci. Lett., 383, 113–122, https://doi.org/10.1016/j.epsl.2013.09.038, 2013.

Zhao, Y., Guo, L., Guo, Z., Chen, Y. J., Shi, L., and Li, Y.: High resolution crustal model of SE Tibet from joint inversion of seismic P-wave travel-times and Bouguer gravity anomalies and its implication for the crustal channel flow, Tectonophysics, 792, 228580, https://doi.org/10.1016/j.tecto.2020.228580, 2020.

640 Zhao, Y., Guo, Z., Wang, K., and Yang, Y. J.: A Large Magma Reservoir Beneath the Tengchong Volcano Revealed by Ambient Noise Adjoint Tomography, J. Geophys. Res., 126, e2021JB022116, https://doi.org/10.1029/2021JB022116, 2021.

Zheng, C., Ding, Z. F., Song, X. D.: Joint inversion of surface wave dispersion and receiver functions. for crustal and uppermost mantle structure in Southeast Tibetan Plateau. Chinese J. Geophys.(in Chinese), 59(9): 3223-3236, doi:
645   10.6038cjg20160908, 2016.

Zheng, X., Zhao, C., Zheng, S., and Zhou, L.: Crustal and upper mantle structure beneath the SE Tibetan Plateau from joint inversion of multiple types of seismic data, Geophys. J. Int., 217, 331–345, https://doi.org/10.1093/gji/ggz027, 2019.

Zhou, L., Zhao, C., Xiu, J., Chen, Z.: Tomography of QLg in Sichuan-Yunnan Zone. Chinese J.Geophys.(in Chinese), 51(6): 1745-1752, 2008.

650 Zhou, L., Zhao, C., Zheng, X., Chen, Z., and Zheng, S.: Inferring water infiltration in the Longtan reservoir area by three-dimensional attenuation tomography, Geophys. J. Int., 186, 1045–1063, https://doi.org/10.1111/j.1365-246X.2011.05124.x, 2011.

Zhou, L.: Attenuation tomography of the earth media, Ph.D. Thesis, Institute of Geophysics, China Earthquake Administration, Beijing, 161-174, 2016.

655 Zhou, L., Zhao, C., Luo, J., and Chen, Z.: A Detailed Insight into Fluid Infiltration in the Three Gorges Reservoir Area, China, from 3D VP, VP/VS, QP, and QS Tomography, Bull. Seismol. Soc. Am., 108, 3029–3045, https://doi.org/10.1785/0120170361, 2018.

Zhou, L., Song, X., Yang, X., and Zhao, C.: Rayleigh Wave Attenuation Tomography in the Crust of the Chinese Mainland, Geochem. Geophys. Geosystems, 21, e2020GC008971, https://doi.org/10.1029/2020GC008971, 2020.

660 Zhu, H., Bozdağ, E., Duffy, T. S., and Tromp, J.: Seismic attenuation beneath Europe and the North Atlantic: Implications for water in the mantle, Earth Planet. Sci. Lett., 381, 1–11, https://doi.org/10.1016/j.epsl.2013.08.030, 2013.

Zou, H., Shen, C.-C., Fan, Q., and Lin, K.: U-series disequilibrium in young Tengchong volcanics: Recycling of mature clay sediments or mudstones into the SE Tibetan mantle, Lithos, 192–195, 132–141, https://doi.org/10.1016/j.lithos.2014.01.017, 2014.

665